

Chapter 1

STUDY OF CRACK DYNAMICS USING THE VIRTUAL INTERNAL BOND METHOD

Patrick A. Klein
and Huajian Gao

It is a great honor for us to contribute to this 60th Anniversary Volume in honor of Professor James R. Rice and to commemorate his profound contributions to the science of fracture. All of us are indebted to him for the leadership he has provided through the excellence of his scholarship as well as the warm and gentle way he has influenced all his students.

—H.G., 1999

Abstract Most existing theories of fracture are based on small deformation constitutive models. These approaches are in contrast to the fact that extraordinarily large, nonlinear elastic deformations inevitably occur during brittle fracture. Though the classical approaches have proved successful in a wide range of applications, they may be inapplicable for or have proved incapable of explaining experimental observations in which nonlinear, hyperelastic material response is an essential feature of the phenomenon. The fracture path instabilities observed during dynamic propagation of cracks are among the phenomena that have not yet been thoroughly explained. Simulation approaches that incorporate a cohesive view of material are able to demonstrate the appearance of crack tip instabilities. Molecular dynamics and cohesive surface methods are among the methods that exhibit this behavior. A virtual internal bond (VIB) model with randomized cohesive interactions between material particles has been proposed as an integration of continuum models with cohesive surfaces and atomistic models with interatomic

bonding. This approach differs from an atomistic model in that a phenomenological “cohesive force law” is assumed to act between “material particles” which are not necessarily atoms. It also differs from a cohesive surface model in that, rather than imposing a cohesive law along a prescribed set of discrete surfaces, a randomized network of cohesive bonds is statistically incorporated into the constitutive response of the material via the Cauchy-Born rule, by equating the strain energy function on the continuum level to the potential energy stored in the cohesive bonds due to an imposed deformation. The approach could be viewed as an attempt to provide a more physical basis for the hyperelastic constitutive laws used in finite strain continuum mechanics. This approach allows the phenomenon of dynamic crack tip instabilities to be analyzed within a continuum framework. Direct simulation of crack growth without a presumed nucleation, growth, or branching criterion lends support to the theory that instabilities occur as a result of a local limiting speed, governed by the rate at which bond-breaking information can be transmitted to the material ahead of a propagating crack.

1. INTRODUCTION

Cracks propagating at high speeds in brittle materials display behavior that the fracture community has yet to find consensus in explaining. Much of the current debate involves the factors that determine the terminal velocity of propagating cracks and the roughened appearance of fracture surfaces produced under fast fracture. The experimental methods used to study dynamic fracture, some key experimental observations, as well as a review of a number of models that attempt to explain the observed phenomena are reviewed by Ravi-Chandar (Ravi-Chandar, 1998). The theoretical limiting speed for crack propagation is the Rayleigh surface wave speed c_R . However, experimental studies of cracks propagating through brittle materials typically quote terminal crack speeds of approximately $c_R/2$, while instabilities have been observed for crack speeds as low as $c_R/3$. Detailed experiments of dynamic crack propagation through the brittle polymer Homalite-100 appear in the studies of Ravi-Chandar and Knauss (Ravi-Chandar and Knauss, 1984a; Ravi-Chandar and Knauss, 1984b; Ravi-Chandar and Knauss, 1984c; Ravi-Chandar and Knauss, 1984d). They observe the well-known “mirror-mist-hackle” appearance of the fracture surface. An image from their study (Ravi-Chandar and Knauss, 1984b) showing the fracture surface is reproduced in Figure 1.1.

The direction of crack propagation is from left to right in the figure. The image shows that the crack surface becomes progressively rougher as the crack extends and the crack speed gets correspondingly higher. By

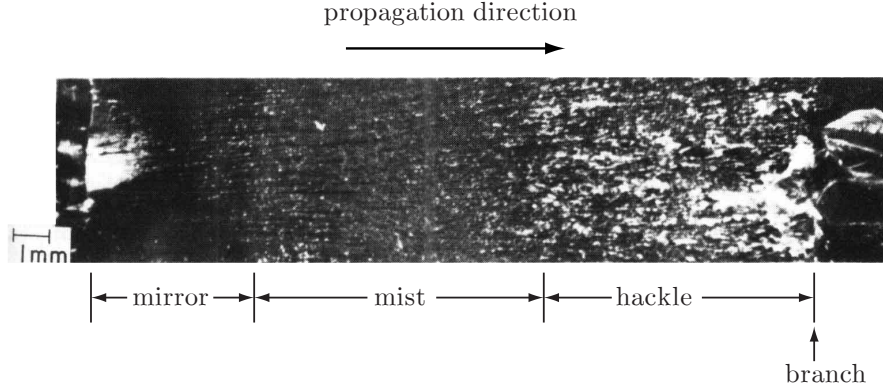


Figure 1.1 “Mirror-mist-hackle” appearance of a fracture surface observed by Ravi-Chandar and Knauss (Ravi-Chandar and Knauss, 1984a; Ravi-Chandar and Knauss, 1984b; Ravi-Chandar and Knauss, 1984c; Ravi-Chandar and Knauss, 1984d).

the method of caustics, they are able to observe distinctly different behavior in the propagating crack front that helps explain the appearance of the fracture surface. In the initial stages of growth, the crack extends by the propagation of a single, curved front, similar to what is observed under quasi-static conditions. The fracture surface appears essentially smooth, leading to its description as the “mirror” zone. As growth progresses, the crack front appears to extend by the action of multiple, smaller crack fronts. The opaque appearance of the crack surface due to fine-scale roughness leads to its description as the “mist” zone. In the “hackle” zone, the scale of the multiple crack fronts increases, leading to a larger degree of fracture surface roughening.

The emergence of crack tip instabilities under dynamic conditions was first predicted analytically in a study by Yoffe (Yoffe, 1951). Her analysis predicts branching at 60° when the propagation speed reaches approximately $0.6 c_R$. Though the result is significant in demonstrating the onset of fracture path instabilities, neither the crack speed nor the branching angle agrees well with experimental observations. Branching angles typically fall between 10° and 45° , while instabilities appear at speeds well below Yoffe’s predicted value. In particular, Fineberg and coworkers (Fineberg et al., 1991; Fineberg et al., 1992) make detailed measurements of crack propagation in PMMA, showing the onset of oscillatory behavior in the crack tip at speeds of roughly $c_R/3$. Classical theories are unable to explain the development of crack tip instabilities at these speeds. It has been suggested by Gao (Gao, 1996; Gao, 1997) that the hyperelastic nature of crack tip deformation may be essential

for understanding dynamic crack tip instabilities. Elastic softening due to hyperelastic stretching can drastically change the way acoustic waves propagate in a solid. The variation in the elastic properties with deformation referred to in this setting should not be associated with models of continuum damage. Damage models attempt to incorporate the effects of microstructural evolution in the behavior of a material, such as microcrack distributions (Kachanov, 1992) or the nucleation and coalescence of voids (Gurson, 1977). The elastic softening under consideration in the present context is an effect of the continuously varying stiffness of a nonlinear cohesive interaction. To illustrate this point, let us consider how a long wavelength signal propagates along an atomic chain stretched toward its cohesive limit. Before the chain is stretched, it behaves like an elastic bar along which a longitudinal wave can be transmitted with speed equal to $\sqrt{E/\rho}$, where E denotes the initial stiffness (Young’s modulus) and ρ the density of the chain. As the chain is stretched near its cohesive (fracture) limit, the tangent stiffness vanishes while a finite tension builds up with magnitude equal to the cohesive stress T_{\max} . At this point, the chain behaves like an elastic string along which a transverse wave can be transmitted with speed equal to $\sqrt{T_{\max}/\rho}$. Note that the cohesive-state wave speed depends on the magnitude of the stress rather than the slope of the stress-strain curve. During this hyperelastic deformation, the slope of the force-displacement (or stress-strain) curve continuously decreases from its initial value corresponding to the elastic stiffness of the chain, and ultimately vanishes at the cohesive limit. Clearly, a linear theory assuming constant stiffness cannot be used to investigate the behavior of the chain near its failure point.

Generalizing the above concept, Gao (Gao, 1996; Gao, 1997) has shown that a homogeneous, isotropic, hyperelastic solid exhibits this string-like behavior near its plane strain equibiaxial cohesive stress in that the cohesive-state wave speed is equal to $\sqrt{\sigma_{\max}/\rho}$, where σ_{\max} is the cohesive stress and ρ is the density of the undeformed solid. The state of plane strain equibiaxial stress resembles the condition that a material particle experiences in front of a mode I crack tip. This observation comes directly from Irwin’s (Irwin, 1957) classic crack tip fields. This cohesive state is identified as the bottleneck state (Gao, 1996) for transmission of fracture signals ahead of a mode I crack tip. The crack propagation velocity is limited by how fast elastic waves can transport strain energy ahead of the crack to sustain the bond breaking processes in the fracture process zone. From this point of view, the cohesive-state wave speed leads to the concept of local limiting fracture speed (Gao, 1996) which has provided an explanation for the “mirror-mist-hackle” instabilities. Assuming values of $\sigma_{\max} = E/30$ and a Poisson’s ratio of

$\nu = 1/4$, the cohesive state wave speed is roughly $0.32 c_R$, which is in good agreement with Fineberg's measurements. Gao's (Gao, 1993) wavy crack model presents a multiscale view of a dynamic crack in which the global, or apparent, crack speed is driven near $c_R/2$ to maximize the fracture energy absorbed by the advancing crack, while the microscopic tip speed may be significantly higher in response to local crack driving forces. A multiscale view may also be helpful in understanding the "mirror-mist-hackle" instabilities as the crack path begins to deviate in an attempt to circumvent the acoustic barrier presented by elastically softened material immediately ahead of the crack. Hyperelastic constitutive models that are capable of describing a material's transition to fracture have not been available for studying these effects. As will be shown, the Virtual Internal Bond (VIB) model displays this cohesive state behavior and should therefore be capable of reproducing dynamic crack tip instabilities.

The atomistic simulations of Abraham and coworkers (Abraham et al., 1994; Abraham, 1997) display dynamic crack instabilities reminiscent of the experimental results though at decidedly smaller length and time scales. The numerical studies of Xu and Needleman (Xu and Needleman, 1994), employing networks of cohesive surface elements, are also successful in producing crack tip instabilities that qualitatively match the experimentally observed behavior. In their study, the continuum elements are modeled using the Kirchhoff-St. Venant constitutive relations, that do not display any softening, while the cohesive surfaces are governed by a traction-separation potential with qualitative features similar to those discussed for the potential in Section 5.. Their observation of instabilities may also be explained with the local limiting speed theory since the "composite" material composed of continuum elements with intervening cohesive surfaces has the effective properties of a cohesive continuum, though with mesh dependent anisotropic characteristics.

2. THE VIRTUAL INTERNAL BOND MODEL

The general features of the VIB model (Gao and Klein, 1998), as well as more detailed study of its localization behavior (Klein and Gao, 1998; Klein, 1999), are described elsewhere. A brief review of the model is repeated here for completeness. The model attempts to incorporate the behavior of a spatial distribution of cohesive bonds that are presumed to act at the microstructural level. The link between the microstructure and continuum-level measures of deformation is made using the Cauchy-Born rule. This approach is employed by Ortiz, Phillips, and Tadmor to

develop constitutive models for single crystal materials (Tadmor et al., 1996). From a practical point of view, it is desirable to extend the procedure for embedding cohesive behavior beyond models for single crystal materials. We would like to develop a model to study fracture in non-crystalline materials, such as polymers or glasses, or in polycrystalline materials for which the elastic anisotropy is lost due to the homogenizing effect of many randomly oriented crystalline grains. The concept of homogenization is applied here to the interactions between particles. The resulting constitutive model embeds the cohesive nature of the interaction potentials, but is free of any orientational dependencies.

The VIB model is developed within the framework of hyperelasticity. The current, or deformed, configuration of a body is described as $\mathbf{x} = \boldsymbol{\varphi}(\mathbf{X})$, by a mapping $\boldsymbol{\varphi}$ of the undeformed configuration \mathbf{X} . The arrangement of cohesive interactions among material particles is described by a spatial bond density function. The strain energy density is computed by integrating the bond density in space in a continuous analog to the sum over discrete lattice neighbors for the case of crystalline materials. The VIB form of the strain energy density function is

$$\Phi = \frac{1}{\Omega_0} \int_{\Omega_0^*} U(l) D_\Omega d\Omega, \quad (1.1)$$

where Ω_0 is the undeformed representative volume, l is the deformed virtual bond length, $U(l)$ is the bonding potential, D_Ω is the volumetric bond density function, and Ω_0^* is the integration volume defined by the range of influence of U . Depending on the range of influence of the bond potential function, the integration volume Ω_0^* may not correspond with the representative volume Ω_0 . This difference may be illustrated for crystalline materials whenever the bond potentials extend beyond the lattice unit cell. This method was first alluded to by Gao (Gao, 1996) as a method for constructing an amorphous network of cohesive bonds by a spatial average. The deformed bond length l is computed from the Cauchy-Born rule, assuming the integration volume Ω_0^* deforms homogeneously as described by a given deformation gradient $\mathbf{F} = \frac{\partial \boldsymbol{\varphi}}{\partial \mathbf{X}}$. In order to avoid questions as to whether the Cauchy-Born rule holds for the proposed microstructure, we consider only bond density functions D_Ω that are centrosymmetric. Under this restriction, the deformation at the microstructural level must be homogeneous in order to maintain the symmetry present in the undeformed configuration. In extending this description from a lattice of discrete bonding interactions to a continuous bond distribution, the invariance in the deformation with respect to translation of our observation point is not limited to positioning the

coordinate origin at crystal lattice sites. All points in the material act as centers of symmetry. From physical considerations, we assume the bonding function U will be relatively short range so that, although the bond density function D_Ω describes the relative particle distribution of the entire body about the observation point, the integration volume Ω_0^* will be on the order of the representative volume Ω_0 . The undeformed virtual bond vector is represented as

$$\mathbf{L} = L \mathbf{\Xi}, \quad (1.2)$$

where L is the reference bond length, and $\mathbf{\Xi}$ is a unit vector in the direction of the undeformed bond. Undeformed bonds are mapped to their deformed configuration \mathbf{l} by

$$\mathbf{l} = \mathbf{F} \mathbf{L}. \quad (1.3)$$

Making use of the right Cauchy-Green stretch tensor, the deformed bond length is

$$l(\mathbf{C}) = L \sqrt{\mathbf{\Xi} \cdot \mathbf{C} \mathbf{\Xi}}. \quad (1.4)$$

Expressed as a function of \mathbf{C} , the deformed bond length transforms objectively by construction. The stress response and tangent moduli are computed from the strain energy density (1.1) using the relations from Green elastic theory (Marsden and Hughes, 1983). Employing

$$\frac{\partial l}{\partial \mathbf{C}} = \frac{L^2}{2l} \mathbf{\Xi} \otimes \mathbf{\Xi}, \quad (1.5)$$

the (symmetric) 2nd Piola-Kirchhoff stress is

$$\mathbf{S} = 2 \frac{\partial \Phi}{\partial \mathbf{C}} = \frac{1}{\Omega_0} \int_{\Omega_0^*} \frac{U'(l)}{l} \mathbf{\Xi} \otimes \mathbf{\Xi} L^2 D_\Omega d\Omega, \quad (1.6)$$

and the material tangent modulus is

$$\mathbf{C} = 2 \frac{\partial \mathbf{S}}{\partial \mathbf{C}} = \frac{1}{\Omega_0} \int_{\Omega_0^*} \left(\frac{U''(l)}{l^2} - \frac{U'(l)}{l^3} \right) \mathbf{\Xi} \otimes \mathbf{\Xi} \otimes \mathbf{\Xi} \otimes \mathbf{\Xi} L^4 D_\Omega d\Omega. \quad (1.7)$$

The modulus (1.7) displays Cauchy symmetry as well as the usual major and minor symmetries of elasticity. This result that an amorphous solid with a random network of cohesive bonds satisfies the Cauchy relation seems to be a generalization of Stakgold's theorem (Stakgold, 1950) to

an amorphous solid. A material particle in an amorphous solid satisfies centrosymmetry in a statistical sense, and the cohesive force law corresponds to a two-body potential.

Since we limit our study to centrosymmetric bond density functions, it is natural to express the strain energy density (1.1) in spherical coordinates as

$$\Phi(\mathbf{C}) = \langle U(l) \rangle = \left\langle U(L\sqrt{\boldsymbol{\Xi} \cdot \mathbf{C} \boldsymbol{\Xi}}) \right\rangle, \quad (1.8)$$

where each bond is characterized by coordinates $\{L, \theta, \phi\}$. For conciseness, we have introduced the notation of a spherical average as

$$\langle \bullet \rangle = \frac{1}{\Omega_0} \int_{-\pi}^{\pi} \int_0^{\pi} \int_0^{L^*} (\bullet) D(L, \theta, \phi) L^2 \sin \theta dL d\theta d\phi, \quad (1.9)$$

where L^* represents the maximum distance over which particles interact. In spherical coordinates, the bond direction vector $\boldsymbol{\Xi}$ can be written as

$$\boldsymbol{\Xi}(\theta, \phi) = \begin{Bmatrix} \sin \theta \cos \phi \\ \sin \theta \sin \phi \\ \cos \theta \end{Bmatrix}. \quad (1.10)$$

The precise definition of $D(L, \theta, \phi)$ is that $D(L, \theta, \phi) L^2 \sin \theta dL d\theta d\phi$ represents the number of bonds in the undeformed solid with length between L and $L+dL$ and orientation between $\{\theta, \phi\}$ and $\{\theta+d\theta, \phi+d\phi\}$. Using this notation, the components of the 2nd Piola-Kirchhoff stress and the material tangent modulus from (1.6) and (1.7) can be represented as

$$\mathbf{S} = \left\langle \frac{L^2 U'(l)}{l} \boldsymbol{\Xi} \otimes \boldsymbol{\Xi} \right\rangle \quad (1.11)$$

and

$$\mathbf{C} = \left\langle L^4 \left(\frac{U''(l)}{l^2} - \frac{U'(l)}{l^3} \right) \boldsymbol{\Xi} \otimes \boldsymbol{\Xi} \otimes \boldsymbol{\Xi} \otimes \boldsymbol{\Xi} \right\rangle. \quad (1.12)$$

There are a few special cases with regard to the bond density function $D(L, \theta, \phi)$:

(1) The case

$$D(L, \theta, \phi) = \delta_D(L - L_0) D_{\theta\phi}(\theta, \phi) \quad (1.13)$$

corresponds to a network of identical bonds of undeformed length L_0 . The Dirac delta function is denoted here with δ_D . A crystal

lattice such as face-centered cubic with interactions limited to only first nearest neighbors can be represented as

$$D(L, \theta, \phi) = D_0 \delta_D(L - L_0) \sum_{m=1}^M \sum_{n=1}^N \frac{1}{\sin \theta} \delta_D(\theta - \theta_m) \delta_D(\phi - \phi_n), \quad (1.14)$$

where D_0 is a scaling constant.

(2) The case

$$D(L, \theta, \phi) = D_{L\theta}(L, \theta) \quad (1.15)$$

represents a transversely isotropic solid. It will be convenient in the subsequent discussion to define a notation for the spatial average under the transversely isotropic case as

$$\langle \bullet \rangle_{L,\theta} = \frac{1}{\Omega_0} \int_0^\pi \int_0^{L^*} (\bullet) D_{L\theta}(L, \theta) L^2 \sin \theta dL d\theta. \quad (1.16)$$

(3) The case

$$D(L, \theta, \phi) = D_L(L) \quad (1.17)$$

yields an isotropic solid with fully randomized internal bonds. We will shortly see that the instantaneous response of this solid becomes transversely isotropic under equibiaxial stretching. The instantaneous response becomes generally anisotropic under finite deformations. The associated average for the isotropic case is

$$\langle \bullet \rangle_L = \frac{1}{\Omega_0} \int_0^{L^*} (\bullet) D_L(L) L^2 dL. \quad (1.18)$$

Selecting the radial bond distribution function as

$$D_L(L) = D_0 \delta_D(L - L_0), \quad (1.19)$$

where D_0 is a constant, implies that all of the bonds in the solid are of the same type, or initial length. The result is a model for amorphous material with nearest neighbor bonding only. With this bond distribution, the strain energy density from (1.8) and (1.9) becomes

$$\Phi = \frac{D_0 L_0^2}{\Omega_0} \int_{-\pi}^\pi \int_0^\pi U(l) \sin \theta d\theta d\phi. \quad (1.20)$$

(4) The case

$$D(L, \theta, \phi) = D_L(L) \delta_D(\theta - \pi/2) \quad (1.21)$$

yields a plane stress, isotropic solid. Unlike the standard plane stress approximation, this model is truly two-dimensional, displaying no out-of-plane deformation or stress. The material can be thought of as being composed of a single sheet of cohesive bonds, or layers of noninteracting sheets, since all of the bonds lie in a single plane. Selecting the radial bond distribution function as

$$D_L(L) = D_0 \delta_D(L - L_0), \quad (1.22)$$

where D_0 is a constant, implies that all of the bonds in the solid are of the same type, or initial length. As was the case in three dimensions, the result is a model for amorphous material with nearest neighbor bonding only. For this case, the strain energy density has the especially simple form

$$\Phi = \frac{D_0 L_0^2}{\Omega_0} \int_{-\pi}^{\pi} U(l) d\phi. \quad (1.23)$$

Though this model may be physically unrealistic, its simplicity makes it useful for both theoretical and numerical investigations of the fracture properties resulting from the VIB approach.

In the sections that follow, we will investigate the stress response and fracture properties exhibited by the VIB model. A majority of the discussion will center on the isotropic model defined above for three and two dimensions by cases (3) and (4), respectively.

3. ISOTROPICALLY ELASTIC PROPERTIES AT INFINITESIMAL STRAIN

We are particularly interested in the properties of an amorphous network of cohesive bonds that is homogeneous and isotropic at small strain. The properties of the model at small strains can be used to fit the model parameters to particular materials. For this case, the bond density function is selected as $D(L, \theta, \phi) = D_L(L)$, and \mathbf{E} , the Green Lagrangian strain, and \mathbf{S} reduce to the strain and stress tensors of linear elasticity: $\mathbf{E} \rightarrow \boldsymbol{\epsilon}$ and $\mathbf{S} \rightarrow \boldsymbol{\sigma}$. Φ can be expanded up to the quadratic term as

$$\Phi(\boldsymbol{\epsilon}) = \left\langle U(L) + \frac{L^2}{2} U''(L) (\boldsymbol{\Xi} \cdot \boldsymbol{\epsilon} \boldsymbol{\Xi}) (\boldsymbol{\Xi} \cdot \boldsymbol{\epsilon} \boldsymbol{\Xi}) \right\rangle, \quad (1.24)$$

where the first order term does not appear since the interaction potential is assumed to satisfy $\langle U'(L) \rangle = 0$ to give a stress-free, undeformed state. This produces the generalized Hooke's law

$$\sigma_{ij} = c_{ijkl} \epsilon_{kl}, \quad (1.25)$$

where the modulus under infinitesimal deformations is related to the cohesive bond distribution by

$$\begin{aligned} \mathbf{c} &= \langle L^2 U''(L) \Xi \otimes \Xi \otimes \Xi \otimes \Xi \rangle \\ &= \langle L^2 U''(L) \rangle_L \int_{\pi}^{-\pi} \int_0^{\pi} \Xi \otimes \Xi \otimes \Xi \otimes \Xi \sin \theta \, d\theta \, d\phi. \end{aligned} \quad (1.26)$$

It can be directly verified that

$$\int_{\pi}^{-\pi} \int_0^{\pi} \Xi_i \Xi_j \Xi_k \Xi_l \sin \theta \, d\theta \, d\phi = \frac{4\pi}{15} (\delta_{ij}\delta_{kl} + \delta_{ik}\delta_{jl} + \delta_{il}\delta_{kj}) \quad (1.27)$$

is a fourth-rank isotropic tensor. The resulting elastic stiffness tensor is

$$c_{ijkl} = \mu (\delta_{ij}\delta_{kl} + \delta_{ik}\delta_{jl} + \delta_{il}\delta_{kj}), \quad (1.28)$$

with shear modulus equal to

$$\mu = \frac{4\pi}{15} \langle L^2 U''(L) \rangle_L. \quad (1.29)$$

The other elastic constants are

$$\lambda = \mu \quad \nu = 1/4 \quad E = \frac{2\pi}{3} \langle L^2 U''(L) \rangle_L, \quad (1.30)$$

where λ and μ are the Lamé constants, ν is Poisson's ratio, and E is Young's modulus. Since a variety of engineering materials display values of Poisson's ratio within a range around 1/4, the Cauchy symmetry exhibited by the VIB model does not represent a significant restriction of the formulation for application to practical analyses.

The results for the plane stress, isotropic bond density function

$$D(L, \theta, \phi) = D_L \delta_D(\theta - \pi/2) \quad (1.21)$$

are quite similar, but the relations for the elastic moduli (1.29,1.30) must be modified to account for the difference in spatial dimensions.

The modulus in the generalized Hooke's law (1.25) is given by

$$\begin{aligned}\mathbf{c} &= \langle L^2 U''(L) \Xi \otimes \Xi \otimes \Xi \otimes \Xi \rangle \\ &= \langle L^2 U''(L) \rangle_L \int_{\pi}^{-\pi} \Xi \otimes \Xi \otimes \Xi \otimes \Xi d\phi.\end{aligned}\quad (1.31)$$

The elastic stiffness tensor has the same form given in (1.28). However, the shear modulus becomes

$$\mu = \frac{\pi}{4} \langle L^2 U''(L) \rangle_L. \quad (1.32)$$

From Cauchy symmetry, the Lamé constants are equal ($\lambda = \mu$), but the relations between the other elastic constants are different from the standard relations of three dimensional elasticity. From the Hooke's law relations in strictly two dimensions, Poisson's ratio, Young's modulus, and the bulk modulus are related to the Lamé constants by

$$\nu = \frac{\lambda}{\lambda + 2\mu}, \quad E = \frac{4\mu(\lambda + \mu)}{\lambda + 2\mu}, \quad \text{and} \quad \kappa = \lambda + \mu. \quad (1.33)$$

Using (1.33), the elastic constants for the plane stress isotropic VIB model are

$$\nu = 1/3, \quad \text{and} \quad E = \frac{2\pi}{3} \langle L^2 U''(L) \rangle_L. \quad (1.34)$$

4. ELASTIC PROPERTIES UNDER PLANE STRAIN EQUIBIAXIAL STRETCHING

The state of plane strain, equibiaxial stretching resembles the deformation a material particle experiences ahead of a mode I crack tip. The elastic properties under such a state of deformation at the cohesive limit of the material have been of key importance in the theory of local limiting fracture speeds (Gao, 1996; Gao, 1997).

For plane strain equibiaxial stretching, the deformation gradient is

$$\mathbf{F} = \begin{bmatrix} \lambda & 0 & 0 \\ 0 & \lambda & 0 \\ 0 & 0 & 1 \end{bmatrix}. \quad (1.35)$$

Under this deformation, the bond length from (1.4),

$$l = L \sqrt{\lambda^2 (\Xi_1^2 + \Xi_2^2) + \Xi_3^2} = L \sqrt{1 + (\lambda^2 - 1) \sin^2 \theta}, \quad (1.36)$$

becomes independent of the in-plane orientation angle ϕ . The components of the 2nd Piola-Kirchhoff stress tensor can be calculated from (1.11) as

$$\begin{aligned}
 S_{11} &= \left\langle \frac{L^2 U'(l)}{l} \sin^2 \theta \right\rangle_{L,\theta} \int_{-\pi}^{\pi} \sin^2 \phi \, d\phi = \pi \left\langle \frac{L^2 U'(l)}{l} \sin^2 \theta \right\rangle_{L,\theta} \\
 S_{22} &= \left\langle \frac{L^2 U'(l)}{l} \sin^2 \theta \right\rangle_{L,\theta} \int_{-\pi}^{\pi} \cos^2 \phi \, d\phi = \pi \left\langle \frac{L^2 U'(l)}{l} \sin^2 \theta \right\rangle_{L,\theta} \\
 S_{33} &= \left\langle \frac{L^2 U'(l)}{l} \cos^2 \theta \right\rangle_{L,\theta} \int_{-\pi}^{\pi} d\phi = 2\pi \left\langle \frac{L^2 U'(l)}{l} \cos^2 \theta \right\rangle_{L,\theta} \\
 S_{23} &= \left\langle \frac{L^2 U'(l)}{l} \sin \theta \cos \theta \right\rangle_{L,\theta} \int_{-\pi}^{\pi} \cos \phi \, d\phi = 0 \\
 S_{13} &= \left\langle \frac{L^2 U'(l)}{l} \sin \theta \cos \theta \right\rangle_{L,\theta} \int_{-\pi}^{\pi} \sin \phi \, d\phi = 0 \\
 S_{12} &= \left\langle \frac{L^2 U'(l)}{l} \sin^2 \theta \right\rangle_{L,\theta} \int_{-\pi}^{\pi} \sin \phi \cos \phi \, d\phi = 0.
 \end{aligned} \tag{1.37}$$

The components of the Cauchy stress are

$$\begin{aligned}
 \sigma_{11} &= \sigma_{22} = S_{11} = S_{22} = \pi \left\langle \frac{L^2 U'(l)}{l} \sin^2 \theta \right\rangle_{L,\theta} \\
 \sigma_{33} &= \frac{1}{\lambda^2} \left\langle \frac{L^2 U'(l)}{l} \cos^2 \theta \right\rangle_{L,\theta} \\
 \sigma_{23} &= \sigma_{13} = \sigma_{12} = 0.
 \end{aligned} \tag{1.38}$$

Note that the equibiaxial stretching results in equibiaxial stress. This is not necessarily true for a crystalline solid and indicates that our representation of an amorphous network of cohesive bonds does respond isotropically.

The nonzero components of the material tangent modulus are obtained from (1.12) as

$$\begin{aligned}
C_{1111} &= \langle C(L, \theta) \sin^4 \theta \rangle_{L, \theta} \int_{-\pi}^{\pi} \sin^4 \phi d\phi = \frac{3\pi}{4} \langle C(L, \theta) \sin^4 \theta \rangle_{L, \theta} \\
C_{2222} &= \langle C(L, \theta) \sin^4 \theta \rangle_{L, \theta} \int_{-\pi}^{\pi} \cos^4 \phi d\phi = \frac{3\pi}{4} \langle C(L, \theta) \sin^4 \theta \rangle_{L, \theta} \\
C_{1122} &= \langle C(L, \theta) \sin^4 \theta \rangle_{L, \theta} \int_{-\pi}^{\pi} \sin^2 \phi \cos^2 \phi d\phi = \frac{\pi}{4} \langle C(L, \theta) \sin^4 \theta \rangle_{L, \theta} \\
C_{1212} &= \langle C(L, \theta) \sin^4 \theta \rangle_{L, \theta} \int_{-\pi}^{\pi} \sin^2 \phi \cos^2 \phi d\phi = \frac{\pi}{4} \langle C(L, \theta) \sin^4 \theta \rangle_{L, \theta} \\
C_{3333} &= \langle C(L, \theta) \cos^4 \theta \rangle_{L, \theta} \int_{-\pi}^{\pi} d\phi = 2\pi \langle C(L, \theta) \cos^4 \theta \rangle_{L, \theta} \\
C_{1133} &= \langle C(L, \theta) \sin^2 \theta \cos^2 \theta \rangle_{L, \theta} \int_{-\pi}^{\pi} \sin^2 \phi d\phi = \pi \langle C(L, \theta) \sin^2 \theta \cos^2 \theta \rangle_{L, \theta},
\end{aligned} \tag{1.39}$$

and from the Cauchy relations

$$C_{1313} = C_{1133} = C_{2233} = C_{2323},$$

where

$$C(L, \theta) = L^4 \left(\frac{U''(l)}{l^2} - \frac{U'(l)}{l^3} \right). \tag{1.40}$$

The components of the elastic modulus in (1.39) exhibit the symmetry of a transversely isotropic material. Therefore, under equibiaxial stretching the initially isotropic solid develops a transversely isotropic instantaneous response.

When the equibiaxial stress reaches the cohesive limit σ_{\max} , the condition

$$\frac{\partial \sigma}{\partial \lambda} = \frac{\partial S}{\partial \lambda} = 0, \tag{1.41}$$

or, equivalently

$$C_{1111} + C_{1122} = 0, \tag{1.42}$$

is satisfied. The following relations can be observed from (1.39):

$$C_{1122} = C_{1212} = \frac{1}{3} C_{1111} = \frac{1}{3} C_{2222}, \quad (1.43)$$

which when combined with (1.42) indicate that all the in-plane components of C_{IJKL} vanish,

$$C_{IJKL} = 0, \quad \text{for} \quad I, J, K, L = 1, 2. \quad (1.44)$$

In order to understand the implications of these results, we introduce some additional concepts from the theory of wave propagation. In Lagrangian coordinates, the equation of elastodynamics at finite deformations is

$$\frac{\partial \mathbf{P}(\mathbf{X}, t)}{\partial \mathbf{X}} = \rho_0 \frac{\partial^2 \mathbf{x}(\mathbf{X}, t)}{\partial t^2}, \quad (1.45)$$

where $\mathbf{P} = \mathbf{F} \mathbf{S}$ is the (nonsymmetric) 1st Piola-Kirchhoff stress tensor and ρ_0 is the density of the undeformed material. A plane wave propagating through the continuum is described by

$$\mathbf{u}(\mathbf{X}, t) = \mathbf{a} \exp[ik(\mathbf{N} \cdot \mathbf{X} - ct)], \quad (1.46)$$

where \mathbf{u} is the displacement of a material particle, k is the wave number, i is $\sqrt{-1}$, c is the wave speed, and \mathbf{N} is the propagation direction defined in the reference configuration. Inserting the plane wave description (1.46) into the equation of motion (1.45) yields

$$[\mathbf{q}(\mathbf{N}) - \rho_0 c^2 \mathbf{1}] \mathbf{a} = \mathbf{0}, \quad (1.47)$$

where

$$q_{ik}(\mathbf{N}) = B_{ijkL} N_J N_L \quad (1.48)$$

is the acoustical tensor. Nontrivial solutions of (1.47) require that the determinant of the coefficient matrix of \mathbf{a} vanish, yielding the characteristic bulk wave speeds from the eigenvalues of $\mathbf{q}(\mathbf{N})$. The effective modulus \mathbf{B} in (1.48) can be expressed in terms of the Lagrangian representation of stress and modulus as

$$B_{ijkL} = \delta_{ik} S_{JL} + F_{iI} F_{kK} C_{IJKL}. \quad (1.49)$$

Using the results for the stress and modulus at the cohesive limit (1.38,1.39,1.44), the speed of elastic waves propagating in the (X_1, X_2) -plane is

$$c_{\text{lim}} = \sqrt{\frac{\sigma_{\text{max}}}{\rho}}. \quad (1.50)$$

This result agrees with the previous analysis of Gao (Gao, 1996; Gao, 1997) but reaches the same conclusion from a different perspective. His analysis only assumes that the material possesses general cohesive properties and is not derived from the description of a particular constitutive model. Note that waves can travel with a different speed in an out-of-plane direction. This issue is not addressed here. The ratio

$$\nu_e = \frac{C_{1122}}{C_{1111}} \quad (1.51)$$

is the plane strain “Poisson’s ratio” at finite deformation. Gao (Gao, 1997) has shown that the cohesive state wave speed is given by (1.50) as long as Poisson’s ratio ν_e does not approach -1 as the cohesive stress is reached. In the present case, ν_e equals $1/3$ irrespective of the magnitude of the strain.

The cohesive state wave speed is intimately connected to the concept of local limiting fracture speed which has been proposed as an explanation for the occurrence of the “mirror-mist-hackle” dynamic crack tip instabilities. The discrepancy between experimental observations of this speed and the established theory of dynamic fracture (Freund, 1990) has been discussed in previous work by Gao (Gao, 1993; Gao, 1996). A close examination of the mode I crack tip deformation suggests (Gao, 1996) that the state of plane strain, equibiaxial cohesive stress is the bottleneck state for transmission of bond breaking fracture signals ahead of a mode I crack. The crack propagation velocity is limited by how fast elastic waves can transport strain energy to material ahead of the crack tip to sustain the bond breaking processes in the fracture process zone. From this point of view, the cohesive state wave speed leads to the concept of local limiting fracture speed at which a straightforward propagation of the crack becomes unfavorable. The crack then attempts to choose an inclined growth direction through material with less elastic softening. Along an inclined direction, stress waves can propagate faster than in the straight-ahead direction where elastic softening has caused all of the in-plane moduli to vanish. As discussed by Gao (Gao, 1993; Gao, 1996), from a global point of view, the apparent crack motion is in a relatively “low inertia” state when the local crack branching occurs. As a result of the local-global inertia competition, the crack chooses to propagate along a wavy path, thus exhibiting the “mirror-mist-hackle” instability. Unlike other descriptions of fracture, this explanation incorporates not only the role of tractions generated as a results of crack opening displacements, but also the effect of deformation-induced variations in material response along the propagation direction. Taking some typical values for the cohesive strength relative to Young’s modulus and Poisson’s ratio as

$\sigma_{\max} = E/30$ and $\nu = 1/4$, we estimate that

$$c_{\text{lim}} \sim 0.32c_R, \quad (1.52)$$

where c_R is the Rayleigh surface wave speed. This is precisely the speed at which crack tip instability is observed experimentally (Fineberg et al., 1991).

The present calculation with amorphous cohesive bonds provides further support for the theory of local limiting fracture speed. It also shows that by introducing the essential features of a cohesive view of material, the present model exhibits the correct cohesive state wave speed and should be suitable for use in numerical simulations of dynamic fracture.

5. A MODEL INTERACTION POTENTIAL

The preceding discussions have not made reference to any particular cohesive potential. For the purpose of demonstration, we introduce the phenomenological cohesive force law

$$U'(l) = A(l - L) \exp\left(-\frac{l - L}{B}\right). \quad (1.53)$$

The defining characteristics of this potential are illustrated in Figure 1.2. The potential has a “well” of depth $U_0 = U(L) = -AB^2$. This quantity can be related to the fracture energy through a J -integral analysis (Klein and Gao, 1998). The response of the potential for bond lengths around the location of this minimum is determined by the parameter A . The “stiffness” at the minimum is $U''(L) = A$. In the left portion of Fig-

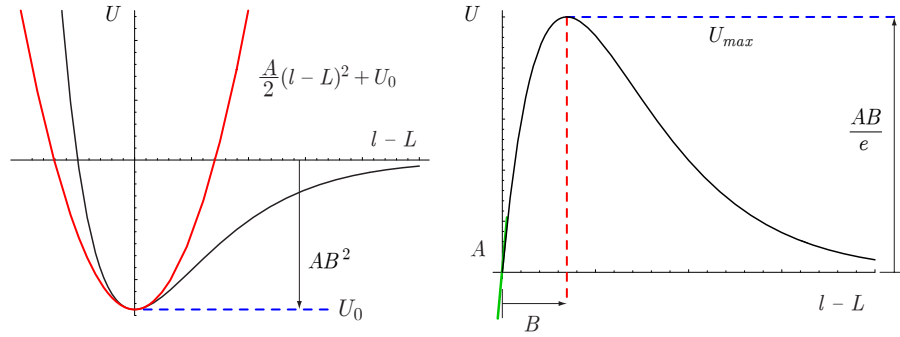


Figure 1.2 Characteristics of the phenomenological cohesive force potential.

ure 1.2, the potential U is shown with a quadratic potential exhibiting the same energy, force, and stiffness at $l = L$. The quadratic potential defines the response of a “linear spring”, for which the force always

varies proportionally with the stretch in the bond. Compared with the quadratic potential, the cohesive potential displays greater stiffness for compressive deformations and the characteristic loss of convexity in tension.

The second parameter B determines the cohesive properties of the potential. The maximum force $U'_{\max} = \frac{AB}{e}$ is generated for a stretched length of $l = L \left(1 + \frac{B}{L}\right)$. In terms of the 2nd Piola-Kirchhoff stress (1.6), we see that the cohesive strength displayed by the VIB model is not determined by the force $U'(l)$, but rather by the ratio $U'(l)/l$. The maximum value for this ratio occurs for

$$l_c = \frac{1}{2} \left(L + \sqrt{4BL + L^2} \right) = L + B + O(B^2/L), \quad (1.54)$$

from which we find

$$\max_l \left[\frac{U'(l)}{l} \right] = \frac{U'(l_c)}{l_c} \approx \frac{AB}{e(1+B)}. \quad (1.55)$$

6. FAILURE INDICATORS

The promise of cohesive modeling is the ability to produce fracture in numerical simulations without requiring an imposed failure criterion. Failure occurs as a natural consequence of the cohesive formulation, which embeds a finite strength and fracture energy in the material model. Although we are not required to impose a failure *criterion*, we do need to identify a failure *indicator*. With classical fracture theory, conditions for crack propagation are posed as a threshold criterion that clearly defines the point at which failure occurs. With a cohesive view of material, failure proceeds in a much more gradual manner. The material does not simply fail, but exhibits a complete history of response from the undeformed state through the cohesive limit to complete failure.

In selecting a failure indicator, we choose to associate it with a threshold condition that corresponds to reaching the cohesive limit rather than a cut-off condition when the stresses being sustained by the material are deemed insignificant. Hill (Hill, 1962) has described the loss of strong ellipticity of the strain energy density function as an indication of the loss of stability of a solid. The analysis is related to the eigenvalues of the acoustical tensor $\mathbf{q}(\mathbf{N})$ (1.48). The loss of strong ellipticity coincides with a loss of uniqueness in the solutions of the governing equation of elastodynamics (1.45). The discontinuous modes of deformation that become admissible with the loss of strong ellipticity appear across a characteristic surface, which we describe with the normal \mathbf{N}^* in the undeformed configuration. With the loss of strong ellipticity produced by models of plasticity exhibiting softening, these characteristic surfaces are

associated with slip, or shear, bands. In the present context, we associate these characteristic surfaces with highly localized bands of deformation that become new crack faces as the material reaches complete failure.

We also study the behavior of a second failure indicator that is related more directly with the cohesive strength than is the analysis of the acoustical tensor. Since the bond density functions of the VIB model are defined with respect to the undeformed configuration, the 1st Piola-Kirchhoff stress \mathbf{P} is related to the force generated by the network of virtual bonds. The maximum values of \mathbf{P} corresponds to the largest forces that can be sustained by the bonds of the virtual microstructure.

The onset of failure indicated by these two criteria as a function of the state of deformation is shown in Figure 1.3 for the plane stress, isotropic VIB model. The configuration of the imposed deformation is

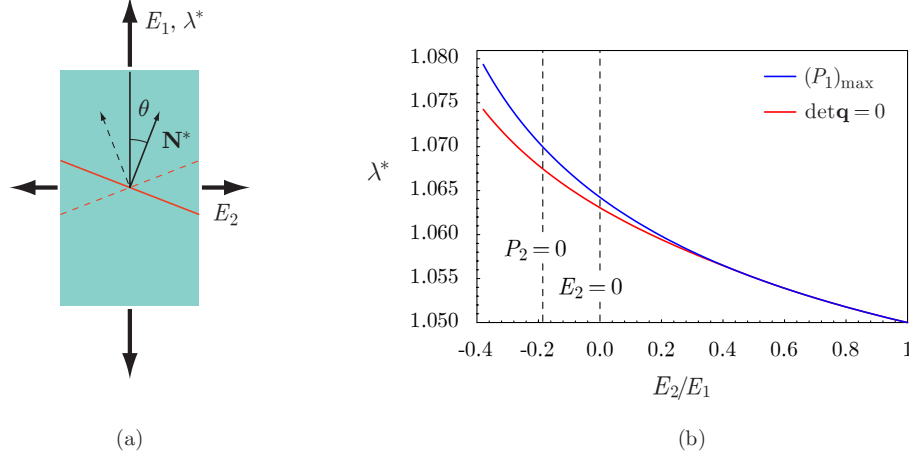


Figure 1.3 (a) Geometry of the loading configuration and (b) a comparison of failure indicators for the plane stress, isotropic VIB model as a function of the state of deformation.

shown in Figure 1.3(a). The deformation is characterized by E_1/E_2 , the ratio of the principal values of the Green strain, where E_1 and E_2 are the strains along and perpendicular to the primary loading direction, respectively. The normal to the characteristic surface associated with the loss of strong ellipticity is shown as \mathbf{N}^* . Figure 1.3(b) illustrates how the two criteria differ in indicating the onset of failure as a function of the state of deformation for $B/L = 0.05$ using the model interaction potential from Section 5.. The stretch in the primary loading direction at the point of failure is designated as λ^* . The deformation states for uniaxial stress ($P_2 = 0$) and uniaxial strain ($E_2 = 0$) are indicated in the figure. For $E_2/E_1 < 0.3$, the loss of strong ellipticity clearly occurs

at a smaller stretch than the stretch required to reach the maximum value of P_1 . In this regime, the maximum value of P_1 attained at λ^* in the figure is unreachable since homogeneous states of deformation become unstable once the acoustical tensor is non-positive definite. As the imposed deformation becomes more nearly equibiaxial, the critical stretches for the two criteria converge. For $E_2/E_1 > 0.3$, the two curves in the figure are nearly indistinguishable. For the equibiaxial case, both criteria indicate the onset of failure at $\lambda^* = B/L$, the stretch for which the bond force is maximal.

Figure 1.4 shows the orientation of the characteristic surface with normal \mathbf{N}^* as a function of the state of deformation. The angle θ^* is measured from the axis of primary loading, as indicated in Figure 1.3(a). States of deformation corresponding to uniaxial stress and strain are in-

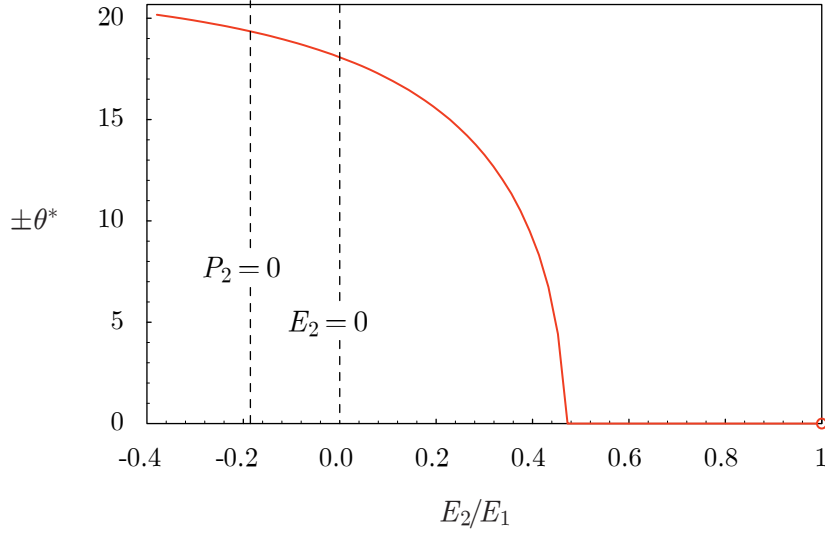


Figure 1.4 Orientation of the localized band as a function of the deformation.

indicated in the figure. The key result of these calculations is that the characteristic surface associated with the loss of strong ellipticity is oriented perpendicular to the primary loading direction for imposed deformations approaching the equibiaxial state, $E_2/E_1 > 0.5$ in the figure. From the asymptotic crack tip solutions of linear elasticity, we know that the state of equibiaxial stretching resembles the deformation a material particle experiences in front of a mode I crack tip. Therefore, it is encouraging that the direction of crack growth indicated by \mathbf{N}^* matches our expectations for the direction of propagation of a mode I crack. Under mixed-mode conditions, classical fracture theory requires that we

postulate a crack propagation direction. Typically, one prescribes crack propagation in the locally mode I direction, the orientation for which $K_{II} = 0$. Alternatively, one could select the direction corresponding to the largest hoop stress $\sigma_{\theta\theta}$ surrounding the crack tip. Since the mechanisms of material failure are not well understood, the most appropriate choice for the direction of crack propagation is also unclear.

With the VIB model, the fracture characteristics under mixed-mode conditions is embedded in the constitutive behavior. Once the parameters in model have been selected, no additional criteria need to be imposed in order to reproduce a wide variety of fracture phenomena. As shown in Figures 1.3 and 1.4, the loss of strong ellipticity appears to be an appropriate indicator of the onset of failure. For loading with mode I character, it agrees with our expectation for failure to initiate as the stress in the material approaches the cohesive limit and for crack propagation to occur in the direction perpendicular to the direction of the largest stress.

7. NUMERICAL SIMULATIONS

In order to demonstrate the capability of the VIB model to reproduce dynamic crack tip instabilities, we present two-dimensional simulations using the plane stress, isotropic VIB model and three-dimensional simulations using the VIB model in principal stretches (Klein, 1999). Details of the VIB model in principal stretches will not be described here, but we note that expressing the model in principal stretches greatly improves computational efficiency for three-dimensional problems. For these calculations, the VIB model is used within an updated Lagrangian finite element formulation. The equations of motion are integrated in time using an explicit, central difference scheme from the classical Newmark family of methods. The geometry of the finite element models is shown in Figure 1.5. As noted in the figure, the three-dimensional model possesses considerably more degrees of freedom although its overall dimensions are smaller. The two-dimensional model contains 159,175 nodes in 158,705 elements for a total of 318,106 degrees of freedom, accounting for the nodes with prescribed kinematic boundary conditions. The three-dimensional model contains 1,305,702 nodes in 1,260,000 elements for a total of 3,865,800 degrees of freedom. The models are loaded by symmetrically prescribed velocity boundary conditions for the nodes along the upper and lower edges of the domains. The boundary nodes are accelerated to the prescribed velocity over a time of $0.2\mu s$, essentially simulating an impact load. Additional boundary conditions are prescribed to prevent rigid body motion. For the three-dimensional sim-

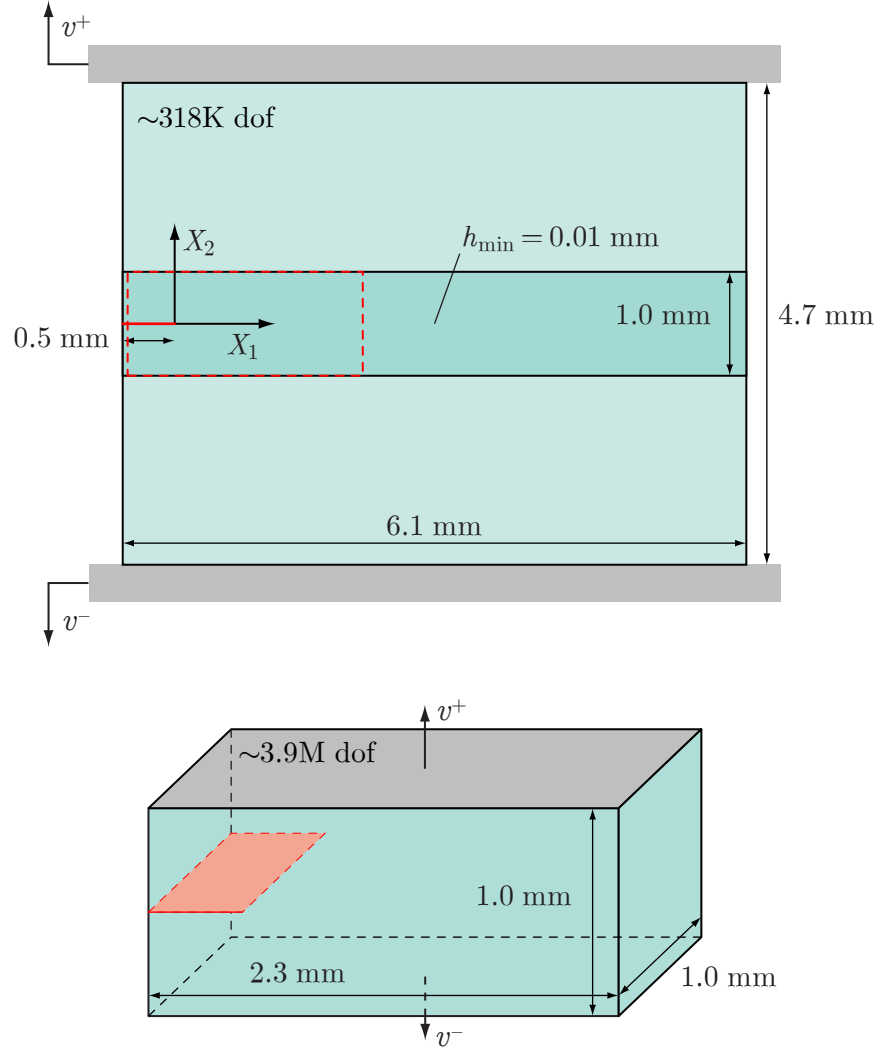


Figure 1.5 Geometry and dimensions of the two- and three-dimensional finite element models used to study dynamic crack tip instabilities. The size of the three-dimensional model is shown on the two-dimensional model with a dashed outline.

ulations, the remaining surfaces are traction-free. The material parameters are selected to be representative of PMMA, the material used in the experiments of Fineberg (Fineberg et al., 1991; Fineberg et al., 1992), with $E = 3.24$ GPa, ν constrained by Cauchy symmetry as described in Section 3., and $\rho = 1200$ kg/m³. These values produce dilatational and shear wave speeds of $c_d = 1740$ m/s and $c_s = 1000$ m/s, respectively, and a Rayleigh wave speed (Freund, 1990) given by

$$c_R = c_s \frac{0.862 + 1.14\nu}{1 + \nu} = 932 \text{ m/s.} \quad (1.56)$$

The fracture energy is selected as 350 J/m^2 , and the cohesive strength is selected as $E/30$. A J -integral analysis can be used to show that the fracture energy depends on mesh size with the current form of the VIB model (Klein and Gao, 1998). The given cohesive parameters dictate that elements in the central region of height 1.0 mm have dimension of $h = 9.2 \mu\text{m}$. A three-parameter potential could be created to allow the elastic properties, fracture energy, and cohesive strength to be selected independently. However, this approach represents only a partial solution to the well-known difficulties associated with simulating strain localization. For the two-dimensional simulations, four-noded quadrilateral elements are used throughout the model. The central region is meshed with a regular arrangement of square elements with dimension $9.2 \mu\text{m}$ while the elements in the outer region increase in size with distance away from the central zone. For the three-dimensional simulations, the entire domain is discretized into a regular, structured grid of eight-noded hexahedral “bricks” with dimension $9.2 \mu\text{m}$.

A pre-crack of length 0.5 mm ensures that propagation is initially directed along the centerline of the model, though its path is not prescribed in any way. The simulation results show that crack growth, instabilities, and branching emerge naturally from the properties of the VIB constitutive model. For the two-dimensional simulations, the apparent length of the crack is monitored by tracking the elements in which the acoustic tensor (1.48) is no longer positive definite. Checking this condition requires searching all wave propagation directions to see if there are any for which the wave speeds vanish. Since the models are constrained to prevent rigid body translations, the crack length is taken as the greatest distance along X_1 between the original crack tip position and the centroids of localized elements in the undeformed configuration. The time step for the explicit integration scheme is selected so that $\Delta t c_d/h = 1/3$, where h is the minimum element size.

With the current state of our simulation procedures, the two-dimensional simulations are better-suited to quantitative study than are the

three-dimensional simulations. Working in two dimensions, we are able to make the computational domains larger, reducing the effect of boundaries on the crack behavior, and analysis of the acoustical tensor requires considerably less effort. For these reasons, quantitative analysis of the two-dimensional simulations is presented, while the results of the three-dimensional simulations are more qualitative. We present results of the two-dimensional simulations for three values of the prescribed boundary velocity, $v_{BC} = \{2.6, 5.2, 10.4\}$ m/s. The crack length as a function of the simulation time for all three cases is shown in Figure 1.6. The

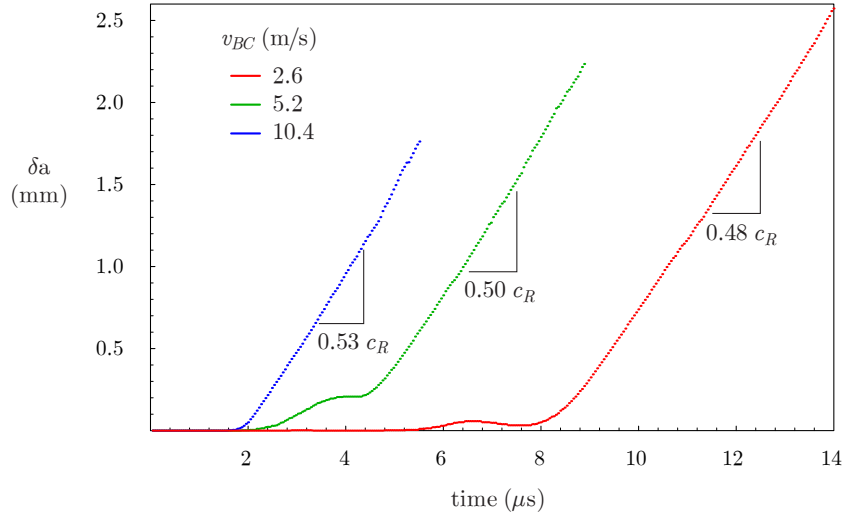


Figure 1.6 Apparent crack length over time for three different values of the imposed boundary velocity.

time to the initiation of crack growth decreases as the impact velocity increases, presumably in response to the time required to generate the critical driving force at the initial crack tip. For the impact velocities of 2.6 m/s and 5.2 m/s, the figure shows that the crack moves forward and then stops before accelerating to the terminal velocity. Based on the dimensions of the model and the dilatational wave speed in the material, the initial loading wave reaches the crack tip from the boundaries after roughly $1.35 \mu\text{s}$. An average terminal velocity is calculated for each case from the slope of the crack length curves $\delta a(t)$ beyond the initial transient behavior. The terminal velocity increases from $0.48 c_R$ to $0.53 c_R$ as the impact velocity increases from 2.6 to 10.4 m/s.

Figure 1.7 shows the crack morphologies for the three cases. Each point along the fracture path marks an element for which the acoustical tensor condition for localization is satisfied at one or more of the element

integration points. The images in the figure actually correspond to superpositions of the fracture path history over the entire simulation time. Since the VIB model is entirely elastic and does not incorporate any

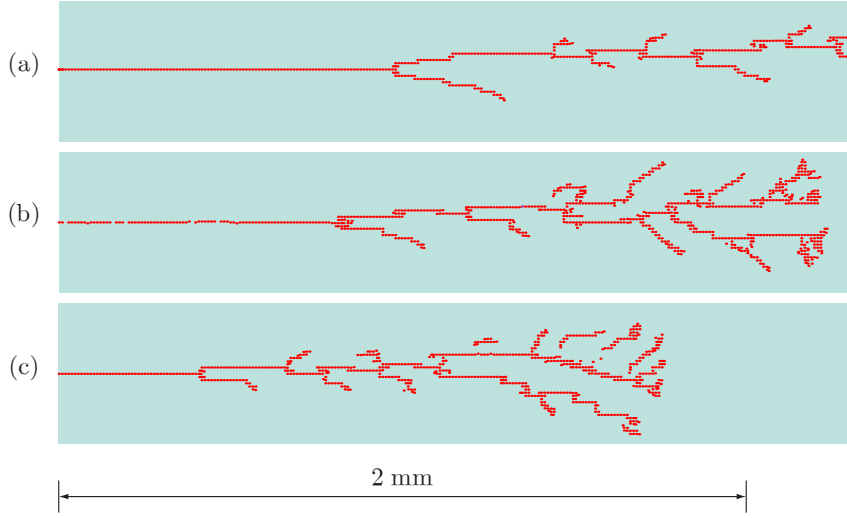


Figure 1.7 Fracture patterns for impact velocities of (a) $v_{BC} = 2.6$ m/s, (b) $v_{BC} = 5.2$ m/s, and (c) $v_{BC} = 10.4$ m/s.

irreversibility in the fracture processes, secondary branches along the fracture path “heal” after the leading edge of the crack has advanced far enough to unload the material in its wake. The fracture paths indicate that the cracks initially propagate straight ahead along the symmetry line of the domain. In each case, the first deviation from straightforward propagation is marked by a symmetric branch at roughly $10\text{--}15^\circ$ to the initial crack plane. This first branch occurs sooner in time and at a shorter crack length as the impact velocity is increased. The subsequent fracture path becomes more irregular as one of the two branches arrests while the other continues to propagate. Once the symmetry of the original propagation has been disrupted, the branches become more irregular. In both Figures 1.7(b) and (c), the branching angles become noticeably larger as the crack advances, reaching a maximum angle of approximately 35° in (b), and reaching almost 55° in (c).

The initial, straight ahead propagation of the crack is “mirror”-like, while the branching at later times forms a “hackle” zone. What is not evident from the fracture paths shown in Figure 1.7 is that some indication of instability appears ahead of the crack tip significantly earlier than the occurrence of the first branch, representing the “mist” mode of propagation. Figure 1.8 shows the arrangement of elements in which

the acoustical tensor condition is met at four instants leading to the first branch in the fracture path for the case of $v_{BC} = 5.2$ m/s. Initially (a), all elements displaying localization lie along a straight path extending from the pre-crack. After $5.1 \mu\text{s}$ (b), the first evidence of localization in elements above and below the symmetry line appears. Based on the

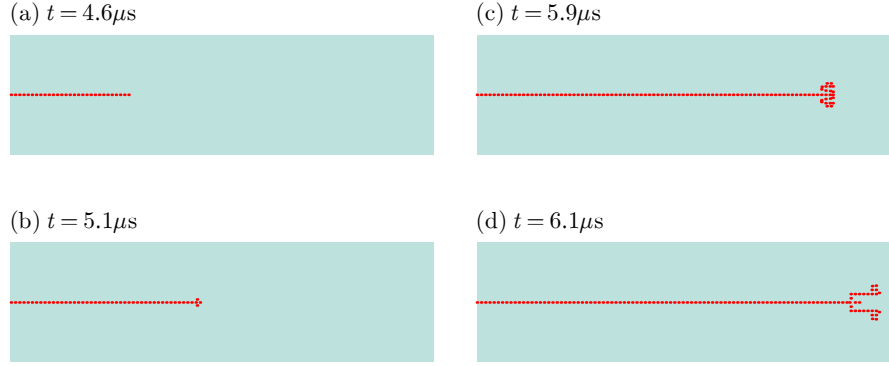


Figure 1.8 The onset of branching for $v_{BC} = 5.2$ m/s.

local limiting speed theory of dynamic crack tip instabilities, the crack has reached a speed at which the strain softened material immediately ahead of the crack is unable to maintain a sufficient rate of energy transfer, and the crack has begun to probe alternate propagation directions. Between 5.1 and $5.9 \mu\text{s}$ after impact (c), the crack continues to accelerate and the acoustical barrier ahead of the crack tip enlarges, evolving to an extended region of “damaged” material. Since deformations in the VIB model are strictly reversible, the material recovers as the tip moves away, leaving no indication of this extended region in the subsequent fracture path. At some time before $6.1 \mu\text{s}$ (d), the crack tip reaches a critical state, and the first true branch appears in the crack path. The sequence of Figures 1.8(a)-(d) bears resemblance to the “mirror-mist-hackle” progression of crack face roughness observed in experiments. The small scale roughness in the numerical results is too fine to be resolved with the current mesh dimensions, but the transition to larger scale roughness is clearly displayed.

The crack length data in Figure 1.6 can be numerically differentiated in order to calculate the apparent crack velocity as a function of time. The crack velocity, normalized by the Rayleigh wave speed c_R , for $v_{BC} = 5.2$ m/s is shown in Figure 1.9. As is evident from the crack length data, the crack moves forward at approximately $2.0 \mu\text{s}$ after the impact occurs, arrests, and then accelerates quickly to an average terminal velocity of approximately $0.5 c_R$. As observed by Fineberg (Fineberg

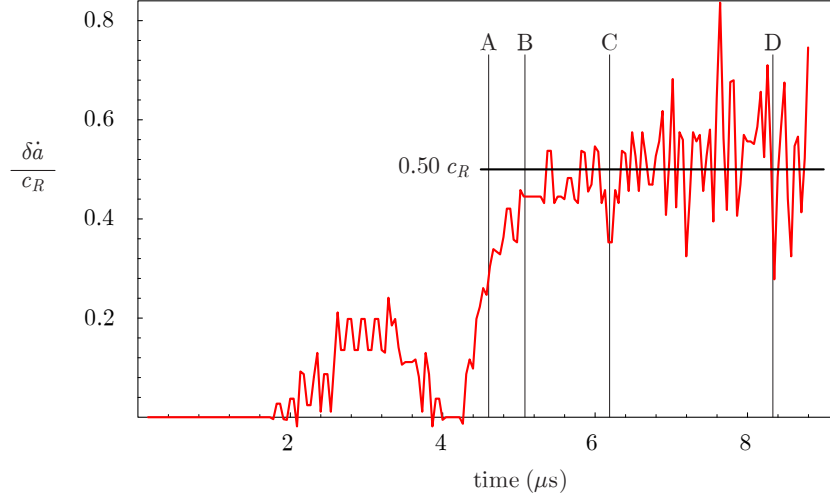


Figure 1.9 Apparent crack velocity $\delta \dot{a}$ over time for an impact speed of $v_{BC} = 5.2 \text{ m/s}$ with markers A-D indicating the times at which the crack is pictured in Figures 1.10-1.13.

et al., 1992), the crack accelerates quickly, but continuously, instead of initiating at the terminal velocity. As the crack accelerates and rapid branching begins, the crack velocity becomes more irregular. This result qualitatively matches the experimental measurements as well as the numerical results obtained by Xu and Needleman (Xu and Needleman, 1994). Markers A-D indicate the times at which the crack is pictured in Figures 1.10-1.13. The four points correspond to (A) initial stages of propagation in the straight-ahead direction; (B) the point at which the small scale instabilities shown in Figure 1.8(b) appear; (C) the point shown in Figure 1.8(d) at which the first clear branch appears; and (D) propagation at the terminal velocity.

Figures 1.10-1.13 show two views of the propagating crack at the four points indicated in Figure 1.9. The upper plot (a) in each figure shows the distribution of the instantaneous shear wave speed c_s for a wave traveling in the X_1 -direction. The contours are normalized by the shear wave speed in the undeformed material $(c_s)_0$. These figures are intended to show how the highly deformed material undergoing fracture is affecting the transfer of crack driving energy to the region ahead of the tip. The shear wave speed also provides a clear indicator of the growing crack. The fracture path is more difficult to identify in the stress plots since elements are not removed from the simulation after the cohesive stress is reached. Stresses, though small, remain continuous across the

crack faces, making the crack path difficult to locate. The lower plots (b) show the distribution of the crack opening stress σ_{22} , normalized by the cohesive stress σ_c . These plots show how the structure of the crack tip stress fields change as the crack propagates through the specimen.

Figure 1.10 shows the crack $4.6 \mu s$ after impact as it accelerates from the arrested state to a speed of approximately $0.3 c_R$. In Fineberg's (Fineberg et al., 1992) results, the crack begins to display oscillatory behavior at this speed. Neither the shear wave speed distribution (a) nor the distribution of σ_{22} (b) shows any signs of crack tip instability. The stress field, with a strong stress concentration marking the current tip position, displays the expected shape similar to the classical tip fields of Irwin (Irwin, 1957). Figure 1.11 shows the crack at $5.1 \mu s$ after impact, the time at which the acoustic barrier shown in Figure 1.8(b) has just started to form. The initial shape of a growing deformation-softened region is evident at the tip of the crack. The crack speed at this instant hovers around $0.4 c_R$. Both the shear wave speed and the stress distribution display waves being emitted from the tip region in a manner that is not present in Figure 1.10. Figure 1.12 shows the crack tip shortly after the initial branch in the fracture path. Both plots in the figure still display a high degree of symmetry. Elastic waves in the wake of the moving tip are even more evident. In the stress plot, the two tips are so close to each other that the combined stress field has a shape which resembles the field of a single tip, though the extent of the highly stressed material is much larger. Clearly, the crack tips are interacting so strongly that crack propagation criteria relying on classic K -field analyses are inapplicable. The final plots in Figure 1.13 show the crack in a late stage of the simulation. Several branches are clearly visible. Both plots display a degree of chaotic behavior as each tip individually seeks a fast fracture path. The highly stressed region ahead of the multiple crack tips extends over a tremendous area, and no resemblance to the classical crack tip fields remains.

Figures 1.14 and 1.15 show the results of the three-dimensional simulations. In each figure, the upper plot (a) shows the distribution of the minimum instantaneous shear wave speed, while the lower plot (b) shows the surface within the domain at which the minimum shear wave speed has dropped to half of the corresponding value in the undeformed material. Figure 1.14 shows the results before the onset of the first branch. A pronounced barrier is visible ahead of the propagating crack. Although the geometry and boundary conditions possess a degree of planar symmetry, the crack is clearly three-dimensional in character. The regions of the crack front approaching the free surfaces trail behind the region of the crack front nearer the center of the domain. Figure 1.14 shows

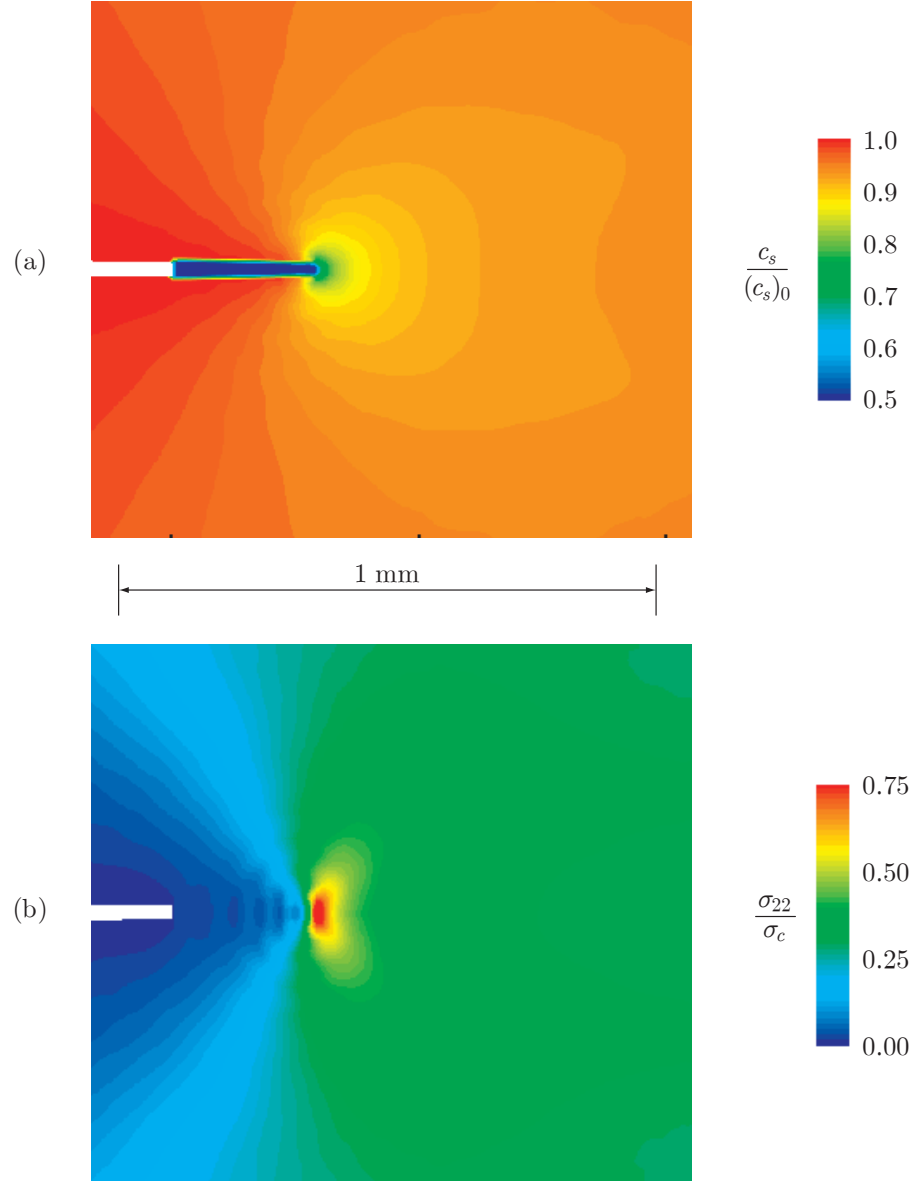


Figure 1.10 4.6 μ s after impact: (a) the distribution of the instantaneous shear wave speed normalized by the initial shear wave speed $(c_s)_0$ of a wave propagating in the X_1 -direction and (b) the distribution of the σ_{22} component normalized by the cohesive stress σ_c , both shown over the deformed domain.

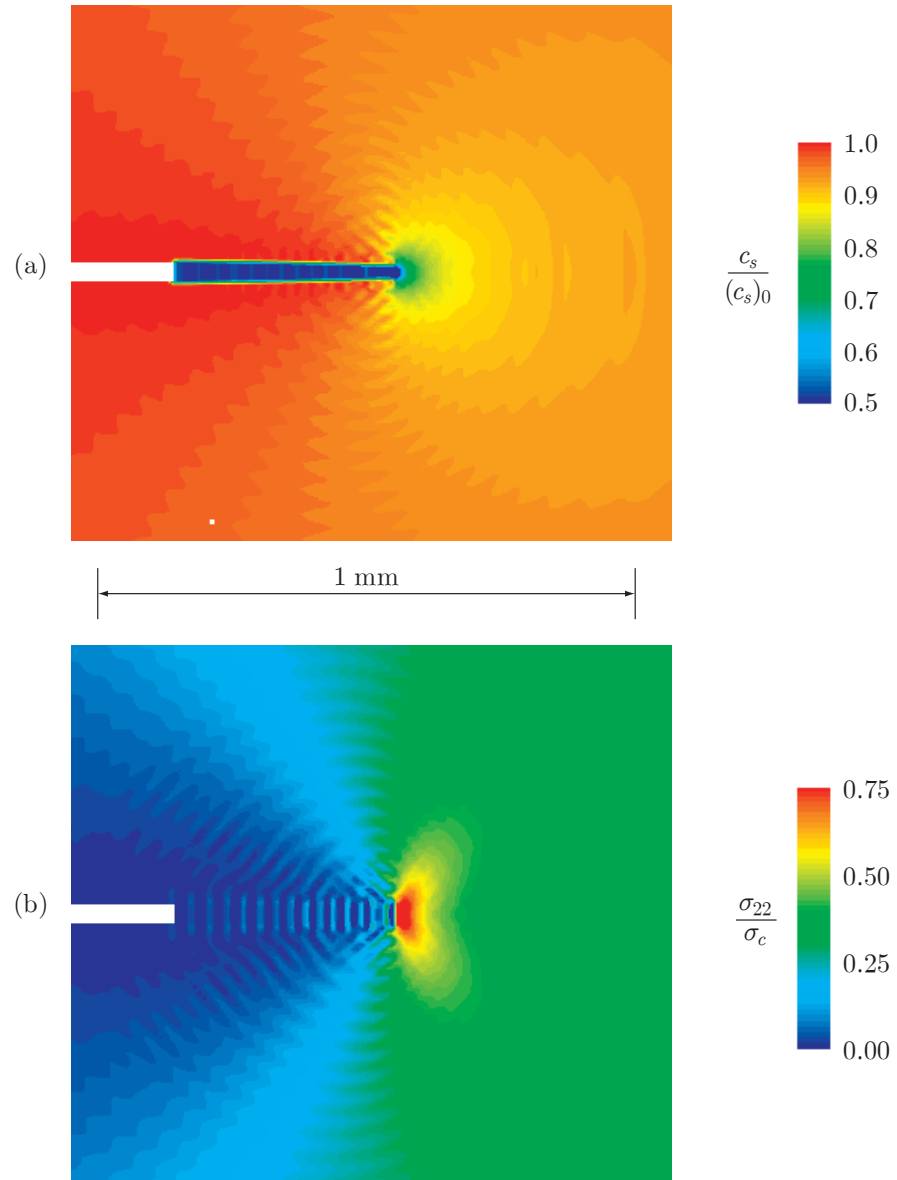


Figure 1.11 Contours of (a) the acoustical shear wave speed and (b) the opening stress $5.1 \mu\text{s}$ after impact.

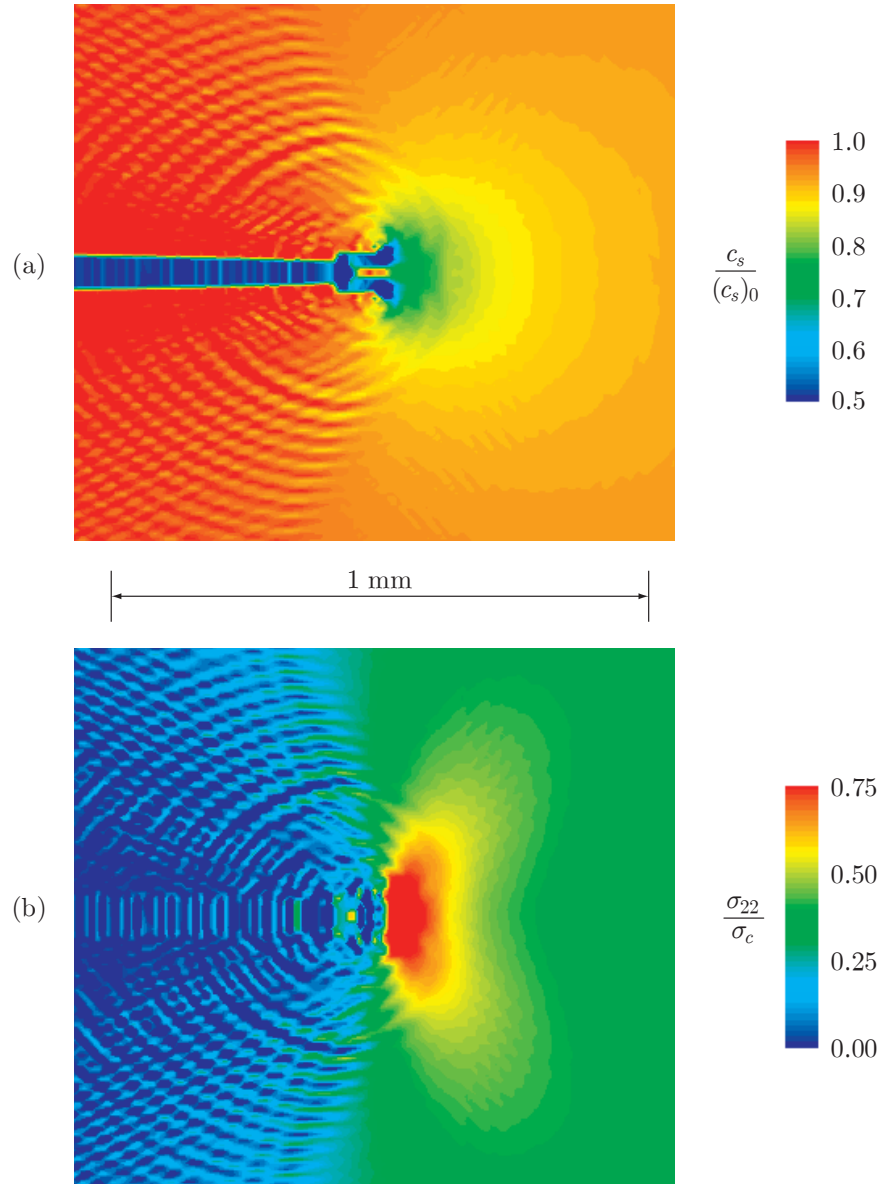


Figure 1.12 Contours of (a) the acoustical shear wave speed and (b) the opening stress $6.2 \mu\text{s}$ after impact.

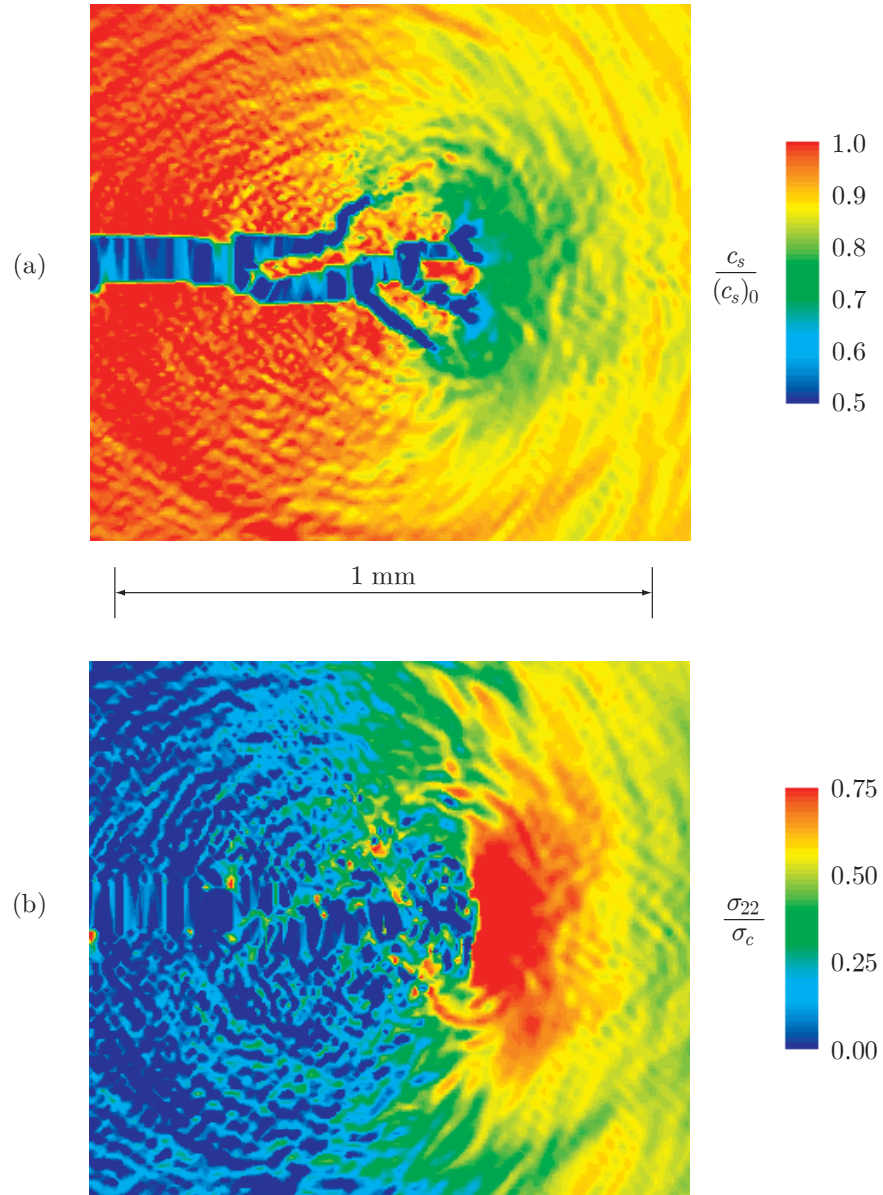


Figure 1.13 Contours of (a) the acoustical shear wave speed and (b) the opening stress $8.3 \mu\text{s}$ after impact.

results shortly after branching has initiated. The first true branches initiate on the free surfaces and propagate inward. The three-dimensional simulations terminate before extensive branching is observed due to difficulties with “mesh tangling”, elements with negative volume produced by extreme deformations.

8. CONCLUSIONS

The simulations of dynamic crack propagation in this section show qualitative agreement with experimental observations of fast fracture. The time-averaged, terminal velocities of crack propagation are clustered around $c_R/2$, though the instantaneous velocity fluctuates rapidly in the range $0.3\text{--}0.8c_R$. Initial instabilities to straight-ahead propagation appear for crack speeds as low as $0.4c_R$, speeds that cannot be predicted using classical fracture analysis. The results provide support for the local limiting speed explanation for the onset of crack tip instabilities. The VIB constitutive model displays a continuous reduction in stiffness as the material is stretched toward the cohesive limit. This elastic softening creates an unstable condition at a rapidly propagating crack tip because the straight-ahead fracture path is blocked by an acoustic barrier to the energy transfer needed to sustain the fracture process. In order to circumvent this barrier, the crack seeks alternate fracture paths, leading to tip oscillations that eventually result in larger scale branching. Notably, the local limiting speed theory does not require the action of micro-cracks, material inhomogeneities, or wave reflections from boundaries in order to explain the appearance of instabilities in the fracture path. Although these effects may contribute to fracture surface roughening in certain cases, they are not strictly required if one adopts a hyperelastic view of the near tip deformations.

Acknowledgments

The authors would like to acknowledge the support provided for this work by the National Science Foundation under Grant #9820988.

References

- Abraham, F. (1997). On the transition from brittle to plastic failure in breaking a nanocrystal under tension (NUT). *Europhysics Letters*, 38:103–106.
- Abraham, F., Brodbeck, D., Rafey, R., and Rudge, W. (1994). Instability dynamics of fracture: a computer simulation investigation. *Physical Review Letters*, 73:272–275.

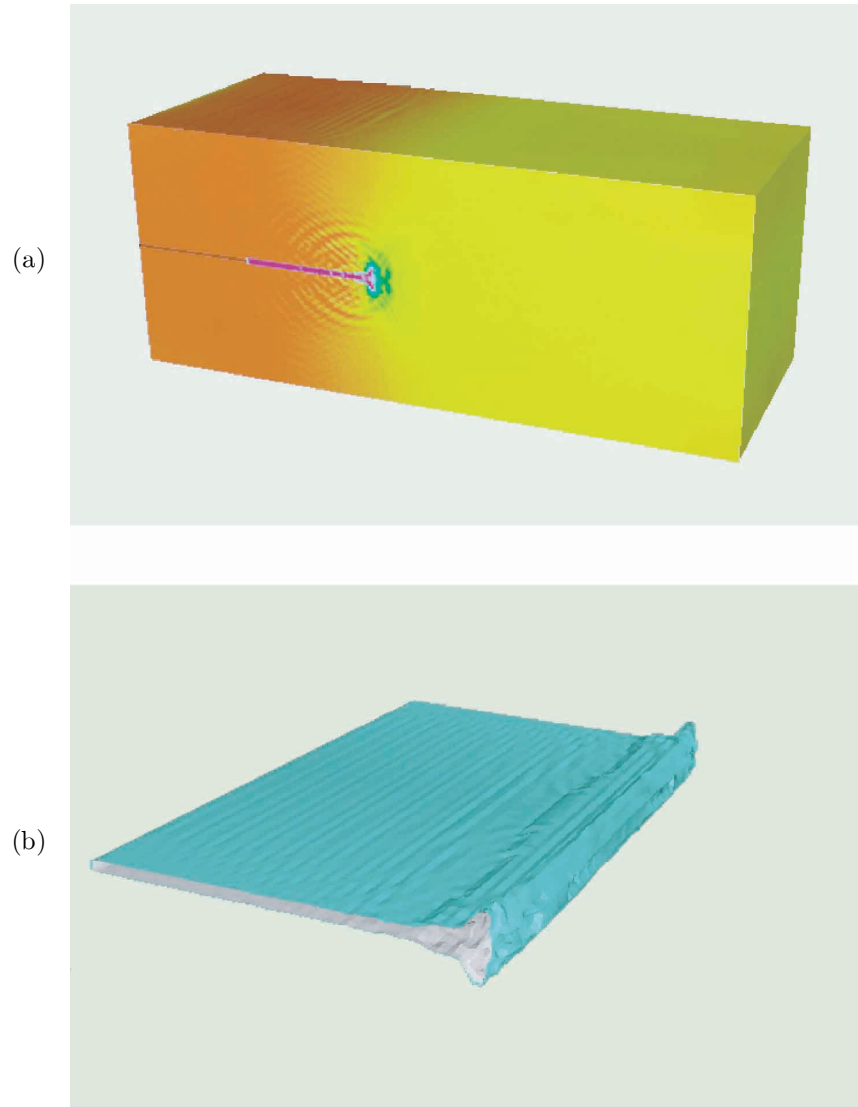


Figure 1.14 The acoustical barrier in three dimensions before branching, $2.7 \mu\text{s}$ after impact.

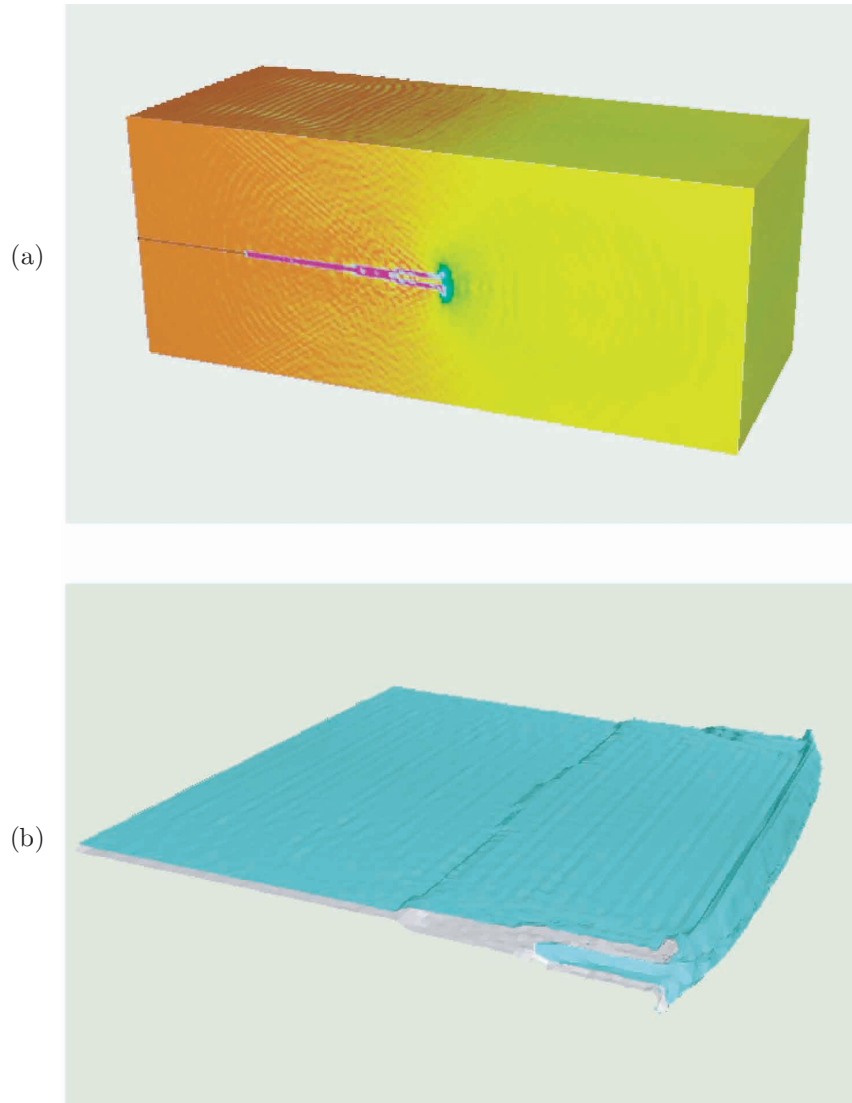


Figure 1.15 The onset of branching in three dimensions $3.2\,\mu\text{s}$ after impact.

- Fineberg, J., Gross, S., Marder, M., and Swinney, H. (1991). Instability in dynamic fracture. *Physical Review Letters*, 67:457–460.
- Fineberg, J., Gross, S., Marder, M., and Swinney, H. (1992). Instability in the propagation of fast cracks. *Physical Review B*, 45:5146–5154.
- Freund, B. (1990). *Dynamic Fracture Mechanics*. Cambridge University Press, New York.
- Gao, H. (1993). Surface roughening and branching instabilities in dynamic fracture. *Journal of the Mechanics and Physics of Solids*, 41:457–486.
- Gao, H. (1996). A theory of local limiting speed in dynamic fracture. *Journal of the Mechanics and Physics of Solids*, 44:1453–1474.
- Gao, H. (1997). Elastic waves in a hyperelastic solid near its plane strain equibiaxial cohesive limit. *Philosophical Magazine Letters*, 76:307–314.
- Gao, H. and Klein, P. (1998). Numerical simulation of crack growth in an isotropic solid with randomized internal cohesive bonds. *Journal of the Mechanics and Physics of Solids*, 46:187–218.
- Gurson, A. (1977). Continuum theory of ductile rupture by void nucleation and growth: PART I. *Journal of Engineering Materials and Technology*, 99:2–15.
- Hill, R. (1962). Acceleration waves in solids. *Journal of the Mechanics and Physics of Solids*, 10:1–16.
- Irwin, G. (1957). Analysis of stresses and strains near the end of a crack traversing a plate. *Journal of Applied Mechanics*, 24:361–364.
- Kachanov, M. (1992). Effective elastic properties of cracked solids: critical review of some basic concepts. *Applied Mechanics Review*, 45:304.
- Klein, P. (1999). *A Virtual Internal Bond Approach to Modeling Crack Nucleation and Growth*. PhD thesis, Stanford University.
- Klein, P. and Gao, H. (1998). Crack nucleation and growth as strain localization in a virtual-bond continuum. *Engineering Fracture Mechanics*, 61:21–48.
- Marsden, J. E. and Hughes, T. J. R. (1983). *Mathematical Foundations of Elasticity*. Dover Publications, Inc., New York.
- Ravi-Chandar, K. (1998). Dynamic fracture of nominally brittle materials. *International Journal of Fracture*, 90:83–102.
- Ravi-Chandar, K. and Knauss, W. (1984a). An experimental investigation into dynamic fracture: I. crack initiation and arrest. *International Journal of Fracture*, 25:247–262.
- Ravi-Chandar, K. and Knauss, W. (1984b). An experimental investigation into dynamic fracture: II. microstructural aspects. *International Journal of Fracture*, 26:65–80.

- Ravi-Chandar, K. and Knauss, W. (1984c). An experimental investigation into dynamic fracture: III. on steady state propagation and branching. *International Journal of Fracture*, 26:141–154.
- Ravi-Chandar, K. and Knauss, W. (1984d). An experimental investigation into dynamic fracture: IV. on the interaction of stress waves with propagating cracks. *International Journal of Fracture*, 26:189–200.
- Stakgold, I. (1950). The Cauchy relations in a molecular theory of elasticity. *Quarterly of Applied Mechanics*, 8:169–186.
- Tadmor, E., Ortiz, M., and Phillips, R. (1996). Quasicontinuum analysis of defects in solids. *Philosophical Magazine A*, 73:1529–1563.
- Xu, X.-P. and Needleman, A. (1994). Numerical simulations of fast crack growth in brittle solids. *Journal of the Mechanics and Physics of Solids*, 42:1397–1434.
- Yoffe, E. (1951). The moving Griffith crack. *Philosophical Magazine*, 42:739–750.